Effect of twist on indentation resistance

DUNCAN, O., CHESTER, M., WANG, W., ALDERSON, Andrew <http://orcid.org/0000-0002-6281-2624> and ALLEN, T.

Materials Today Communications 35 (2023) 105616

Contents lists available at ScienceDirect

Materials Today Communications

journal homepage: www.elsevier.com/locate/mtcomm

Effect of twist on indentation resistance

O. Duncan [a,*], M. Chester [b], W. Wang [a], A. Alderson [c], T. Allen [a]

[a] Department of Engineering, Manchester Metropolitan University, Manchester, UK
[b] PrintCity, Manchester Metropolitan University, Manchester, UK
[c] Materials and Engineering Research Institute, Sheffield Hallam University, Sheffield, UK

ARTICLE INFO

Keywords:
Mechanical metamaterial
Continuum mechanics
Finite-element modelling (FEM)
Mechanical testing

ABSTRACT

With mechanical metamaterials that display force-torque coupling receiving recent attention, we tested the effect of twist on indentation resistance. We hypothesised that the force required to indent a twisting lattice to a set depth would increase with the amount of transverse deformation caused by twist. Based on previous work, various chiral lattices were designed to twist by up to 1.3° per 1 % compression. These lattice designs were 3D-printed in Nylon-12, then tested, with the experiments replicated in finite element simulations. Indentation resistance increased with twist; the lattice with maximum twist required ~70 % higher indentation force (when normalised to compressive stiffness) than the non-twisting (antichiral) one during spherical indentations to 1 % of sample thickness. Further, we calculate the expected effects of twist on indentation resistance by combining the established micropolar and Willis' plane stress moduli with classical Hertzian indentation equations. We found reasonable agreement (within 10 %) between 2D calculation methods use here and previous 3D calculation methods. The indentation resistance calculated using the micropolar plane stress modulus followed the same trends as the simulations and experiments. The calculated indentation force was within 10 % of the simulations and experiments.

1. Introduction

New counterintuitive hardening mechanisms (e.g., [1–8]) are interesting where comfort, energy absorption, or structural integrity are important. Applications of counterintuitive hardening mechanisms include defence [4], medical devices [9], sports equipment [10], aerospace and automotive sectors [11], to name a few [12]. Hardness is a measure of indentation resistance. During indentation with a rigid indenter, a soft substrate deforms axially and transversely. So, the hardness (H) of most isotropic materials increases with Young's modulus (E) and the magnitude of Poisson's ratio (ν) [3,10,13,14]:

$$H \propto \left(\frac{E}{1-\nu^2}\right)^x \tag{1}$$

whereby x is related to indenter shape (2/3 for a spherical indenter). The term inside the brackets is the effective modulus ($\tilde{E}$) [14–16]:

$$\tilde{E} = \frac{E}{1-\nu^2} \tag{2}$$

Hardness is mean pressure in a contact area at a set depth [17–21], while Hertzian (spherical) indentation force (F) is [20,21]:

$$F = \frac{4}{3}\sqrt{Rh^3}(\tilde{E}) \tag{3}$$

whereby h is indentation depth, and R is the radius of the indenting sphere.

Eqs. (1) and (3), and others for Hertzian indentation, can be derived using the method of dimensionality reduction – whereby an axisymmetric three-dimensional (3D) system is represented by a system of one-dimensional components [15,22,23]. During an indentation between a rigid indenter and an elastic half-space, with dimensionality reduction the half-space is represented by a 2D plane [15,22,23]. The effective modulus of the elastic half space ($\tilde{E}$, Eq. 2) is the two-dimensional (2D) plane stress modulus [17,21,24,25].

Counterintuitive hardening mechanisms include auxetics (negative Poisson's ratio) [1–3], shear thickening materials [4–7], and chainmail inspired materials [8]. Isotropic auxetic material can be harder than equivalent stiffness conventional materials [1–3], according to Poisson's ratio limits (of $-1 < \nu < 0.5$ [17]) and Eqs. (1) to (3). So, an auxetic material can be relatively soft to maximise deformation (and minimise

* Corresponding author.
E-mail address: O.Duncan@mmu.ac.uk (O. Duncan).

https://doi.org/10.1016/j.mtcomm.2023.105616
Received 21 November 2022; Received in revised form 27 January 2023; Accepted 10 February 2023
Available online 17 February 2023

peak force) while gradually decelerating impacting bodies during blunt impacts, but can still reduce penetration by concentrated loads. Auxetics are a class of counterintuitive hardening mechanism, based on Cauchy continuum mechanics/classical continuum theory [17], that have received sustained attention since they were first made [26].

The constitutive equation, in classical (Cauchy) elasticity is [17]:

$$\sigma_{ij} = C_{ijkl}\varepsilon_{kl} \tag{4}$$

whereby σ_{ij} is the stress tensor (units Pa), C_{ijkl} is the rank 4 stiffness tensor (units Pa, with i, j, k and l equating to the axes 1, 2 or 3) and ε_{kl} is the dimensionless strain tensor (with $\varepsilon_{kl} = \varepsilon_{lk}$). Cauchy's assumption that strain energy is stored in materials by symmetric linear deformation following application of a uniaxial load is sometimes false [27–29]. Some materials and structures, including some chiral (non-symmetric) mechanical metamaterials [30,31], bone [30,31], and composite turbine blades [32–34], twist internally and externally during extension or compression. In some cases, an internal unit cell can twist, which can cause an externally visible twisting response (e.g., [30,31]). Twist can also be more subtle, occurring around the junction between cell ribs (e.g., [30,31]). While twist around small internal structures is more common, extreme and externally visible twist allows development and validation of theories to explain it.

Twist has recently received attention following its rational design [30,31]. Twist can be explained using the Cosserat/micropolar continuum [27,29,35], and the Willis continuum [36–38]. These theories introduce homogenisations as internal asymmetric length scales tend towards the size of the applied deformation zone. Cosserat and micropolar theories are similar – but in Cosserat theory, the microrotation was not originally connected to applied displacement [29,39–41]. Micropolar theories for solid materials typically assume the rotating units are bonded and the macrorotations can be calculated from the microrotations and displacements [30,39,42]. The constitutive equations for the micropolar continuum are [30,42]:

$$\sigma_{ij} = C_{ijkl}\,\varepsilon_{kl} + D_{ijkl}\,\Phi_{kl} \tag{5}$$

and,

$$M_{ij} = A_{ijkl}\,\Phi_{kl} + B_{ijkl}\,\varepsilon_{kl} \tag{6}$$

whereby A, B and D are additional generalised rank 4 tensors ($B_{ijkl} = D_{klji}$), M is the couple stress tensor, and Φ is the rotational strain tensor.

An alternative to micropolar continuum, also capable of explaining the effects of twist, is Willis continuum [36–38]. While this theory contains dynamic and motion tensors, here we consider only the static, homogenised case – with the constitutive equation [38]:

$$\nabla \bullet \sigma = \nabla \bullet (C : \epsilon) - \alpha \nabla \times \mathrm{u} \tag{7}$$

Whereby α describes asymmetry (units Pa/m) and has been estimated to fit microstructurally faithful simulations, while u is the displacement vector.

Indentation of micropolar materials has been considered before (e.g., [43–47]). These works typically formulate contact pressure and radius (via local stress in 3D), to amend the equations for contact force [46]. Focussing on pressure rather than force, these works do not exclude calculation of contact force via the micropolar 2D plane stress modulus and method of dimensionality reduction [22].

The method of dimensional reduction is the simplest and most intuitive form of indentation analysis. If shown to be valid for twisting materials, it could allow an intuitive demonstration of the effect of twist on indentation resistance while simplifying analysis methods. Application of the method of dimensional reduction requires an axisymmetric indenter, and an isotropic (or transversely isotropic) elastic half-space [15,22,23]. Introducing twist into indentation analysis requires some adaption of the equations relating to the elastic half-space (Eq. 2), possibly the application of micropolar [29,48] or Willis formulations of the 2D plane stress moduli [38]. While twist causes a non-axisymmetric deformation direction (opposite on either side of the indenter), the magnitude and resultant strain energy density are equal. So, it is useful to investigate whether results of analysis based on the method of dimensional reduction are comparable to experimental or microstructurally faithful finite elements simulation results.

In this study, we test the hypothesis that twist, which translates axial to transverse deformation [30,31], would provide a hardening mechanism analogous to Poisson's ratio (Eqs. 1 to 3). To test this hypothesis, we develop the method of dimensional reduction to include plane stress moduli that include twist; the micropolar continuum [27,29,35] and the static variant of Willis continuum [36–38]. We use the established mathematical approach in the method of dimensional reduction to represent surface deformation [15,16,21,22,43–47], and the material's micropolar 2D plane stress modulus to calculate contact force [15,16,21,22], then investigate a simpler 2D plane stress approximation using Willis continuum [38]. We compare these analytical results to 3D analysis methods from the literature [46], and experimental and finite element indentations of previously developed designs of mechanical metamaterials with varying amounts of twist [30].

2. Methods

2.1. Micropolar continuum model

With classical indentation response reliant upon a representative 2D plane [15,22,23] represented by the 2D plane stress modulus (Eqs. 1 to 3), we tested whether such a relationship can be amended to include twist. The stiffness matrix for the micropolar 2D plane stress problem is [29,48]:

$$\begin{pmatrix} \sigma_{11} \\ \sigma_{22} \\ \sigma_{12} \\ \sigma_{21} \\ M_{13} \\ M_{23} \end{pmatrix} = \frac{E_m}{1-\nu_{m^2}} \begin{pmatrix} 1 & \nu_m & 0 & 0 & 0 & 0 \\ \nu_m & 1 & 0 & 0 & 0 & 0 \\ 0 & 0 & \frac{1-\nu_m}{2(1-N^2)} & \frac{(1-\nu_m)(1-2N^2)}{2(1-N^2)} & 0 & 0 \\ 0 & 0 & \frac{(1-\nu_m)(1-2N^2)}{2(1-N^2)} & \frac{1-\nu_m}{2(1-N^2)} & 0 & 0 \\ 0 & 0 & 0 & 0 & 2l_c{}^2(1+\nu_m) & 0 \\ 0 & 0 & 0 & 0 & 0 & 2l_c{}^2(1+\nu_m) \end{pmatrix} \begin{pmatrix} \varepsilon_{11} \\ \varepsilon_{22} \\ \varepsilon_{12} \\ \varepsilon_{21} \\ \Phi_{1,3} \\ \Phi_{2,3} \end{pmatrix} \tag{8}$$

Herein, the "11" axis is aligned to the direction of indentation. The micropolar length scale (l_c) previously used for chiral lattices similar to those we use here was 188 μm [30]. As we used lattices with 50 times larger (25 mm sided) unit cells and external dimensions, l_c was increased (by a factor of 50) to 9.3 mm. For these indentations with a contact radius ($a \approx \sqrt{2Rh} \approx 5.9$ mm) less than 46.5 mm ($a < 5\, l_c$), modification of the lattice response would be required [46]. Φ is the twist angle per axial strain. E_m and ν_m, micropolar Young's moduli and Poisson's ratio [35], were obtained here by finite element simulations. The coupling constant (N) can be calculated from shear and torsional moduli:

$$N = \sqrt{\frac{k}{2(G_m + k)}} \tag{9}$$

whereby k is a micropolar modulus [29]:

$$k = 2(G_m - G_t) \tag{10}$$

while G_t was measured torsional modulus, and shear modulus (G_m) was [29,35,48]:

$$G_m = \frac{E_m}{2(1 + \nu_m)} \tag{11}$$

Assuming axisymmetric twist that can be homogenised in 2D, while considering loading in the vertical 11-axis ($\varepsilon_{22} = -\nu \times \varepsilon_{11}$, $\varepsilon_{12} = (\varepsilon_{11} - \varepsilon_{22})/2 + \phi_{2,3}$, $\varepsilon_{21} = (\varepsilon_{11} - \varepsilon_{22})/2 - \phi_{2,3}$, $\phi_{1,3} = \phi_{2,3}$, and ϕ was measured), all micropolar plane force and torque stresses can be calculated by expanding Eq. (8). The strain energy density (U_m) is [17]:

$$U_m = \frac{\sigma_i \varepsilon_i}{2} + \frac{M_i \Phi_i}{2A} \tag{12}$$

using the Einstein summation. Couple stresses (M_i) were divided by the unit cell cross sectional area (A) to maintain the units of U_m (J/m^3, or N/m^2). Dividing couple stress by unit cell cross sectional area allows recovery of Cauchy mechanics when many unit cells are used, and the energy to twist each one increases (Eq. 8). The micropolar plane strain modulus ($\tilde{E}_m$) is:

$$\tilde{E}_m = \frac{U_m}{\varepsilon_{11}} \tag{13}$$

So, Eq. 3 becomes:

$$F = \frac{4}{3}\sqrt{Rh^3}(\tilde{E}_m) \tag{14}$$

With clear steps to calculate $\tilde{E}_m$ (Eqs. 4 to 9), Eq. (10) could provide a method to calculate (and tune) the indentation resistance of materials that twist. To verify the micropolar 2D plane stress modulus calculation method (Eq. 14) using theoretical 3D calculation data [46], we set h/R to 0.01, G_m and R to unity, and vary l_c between 0 and 0.5. The coupling constant N is proportional to $\sqrt{l_c}$, while in the absence of unit cells in the study in the literature we set $A = \pi l_c^2$. We then vary Φ from zero to the product of 1.5° per % strain (the approximate limit found in this work) and $(1\text{-}\nu_m^2)$, with ν_m set to 0 and 0.5.

2.2. Willis continuum model

The Willis variant of the representative 2D plane [15,22,23], and 2D plane stress modulus, can be formulated from [38]:

$$\begin{pmatrix} \sigma_{11} \\ \sigma_{22} \\ \sigma_{12} \\ \sigma_{21} \end{pmatrix} = \frac{E_m}{1 - {\nu_m}^2} \begin{pmatrix} 1 & \nu_m & 0 & 0 \\ \nu_m & 1 & 0 & 0 \\ 0 & 0 & 1 - \nu_m & \alpha \\ 0 & 0 & \alpha & 1 - \nu_m \end{pmatrix} \begin{pmatrix} \varepsilon_{11} \\ \varepsilon_{22} \\ \varepsilon_{12} \\ \varepsilon_{21} \end{pmatrix} \tag{15}$$

We use the same strain conventions as above. As in previous work by Kadic et al. [38] using similar lattices, we arbitrarily set l_w/L (Willis length scale/ lattice width) as $\phi \times L/9$ (using radians), based on the relationships in Fig. 3 and 4a of reference [38]. We also calculated α as $n^2 \times G_m \times l_w/L$, where n is the number of unit cells per side. This relationship was again derived from Kadic et al. (Eq. 15 in reference [38]). We included the multiplier n^2 based on the varying number of unit cells, as Kadic et al., used 3 by 3 lattices throughout. So, strain energy density and plane stress modulus can (again) be calculated – based on the following variants to Eqs. (13) and (14):

$$\tilde{E}_w = \frac{U_w}{\varepsilon_{11}} \tag{16}$$

$$F = \frac{4}{3}\sqrt{Rh^3}(\tilde{E}_W) \tag{17}$$

whereby the subscript W denotes Willis values.

2.3. Experimental methods

Six chiral and antichiral lattices, based on work by Frenzel et al. [30], were designed in computer aided design software (SolidWorks, 2020, Dassault Systèmes SOLIDWORKS Corp., USA) and 3D-printed in Nylon-12 (selective laser sintered, Formlabs, Fuse 1 - Supplementary information S1 and S2). Powder was mixed at a refresh rate of 30–70 %, heated to 200 °C, then sintered using a 10 W Ytterbium Fiber laser (200 μm spot size, 110 μm layer height). Lattices were post processed by manual brushing and bead blasting with compressed air and abrasive blast beading media (Guyson, Euroblast 4).

The chiral lattices (Fig. 1a) had various rib angles (θ); 34.3° (tangent to the outer circle and the maximum possible value), 30°, 25°, 20° and 10°. The rib angle was 0° for the antichiral lattice (Fig. 1b). The cubic chiral unit cells were asymmetric (Fig. 1c), causing twist in compression, with the amount of twist increasing with θ. As the antichiral lattices (Fig. 1d) were symmetric they did not twist [30]. Mass increased with θ; the 34.3° chiral lattice was ~10 % heavier than the antichiral one. Ideally, during indentation testing (ASTM D3574 – 11 - [49]), many unit cells would contact an indenter, with the length of sample sides close to double the indenter diameter. To give high twist, which reduces with more unit cells [30], lattices consisting of three by three by three cubic unit cell were predominantly used here (25 mm sides for each cell, equating to ~71 mm sides for the lattice).

To facilitate indentation testing, a uniform sheet (1.5–1.6 mm thick) replaced the top layer of 2D extrusions. Top sheet thickness was varied to maintain constant bending stiffness relative to the lattice 2D extrusion (Supplementary information S5). These top sheets were printed and modelled as part of the lattice, so were also present during compression tests. Fillets of radius 0.25 mm were applied under the sheet – where cell ribs otherwise caused sharp angles (≤ 45°), and 0.5 mm radius fillets were applied to all ≤ 45° angles in the unit cells (Fig. 1a & b). The 1.5–1.6 mm thick top sheets had a bending modulus 2.6–2.7 times that of the 2D cell they replaced (Fig. 1a & b), corresponding to the normalised second moment of area I_N. The critical length in micropolar solids relates to the radius the microstructure bends or twists around. For the structures used here, the bending and twisting length were

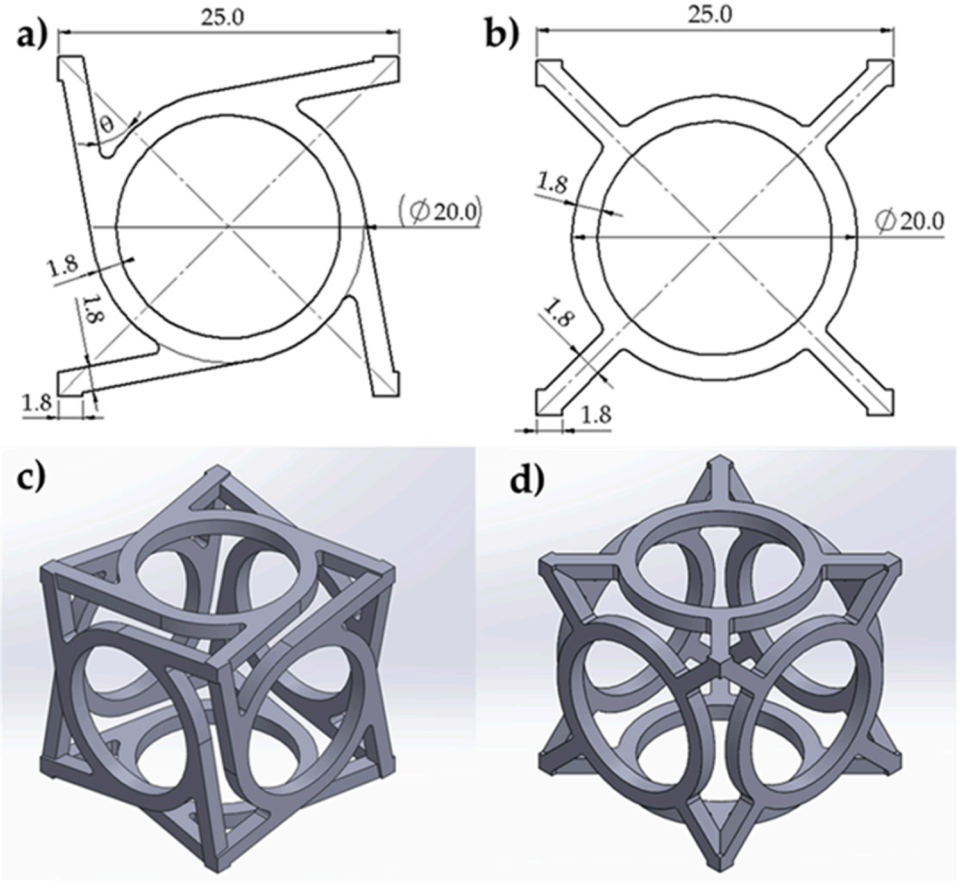

Fig. 1. Dimensions (in mm) of 2D a) Chiral ($\theta = 34.3°$), and b) antichiral ($\theta = 0°$) extrusions (thickness 1.8 mm) that were rotated around the central y- and z-axes to create isotropic, cubic; c) chiral and d) triaxial symmetric antichiral unit cells.

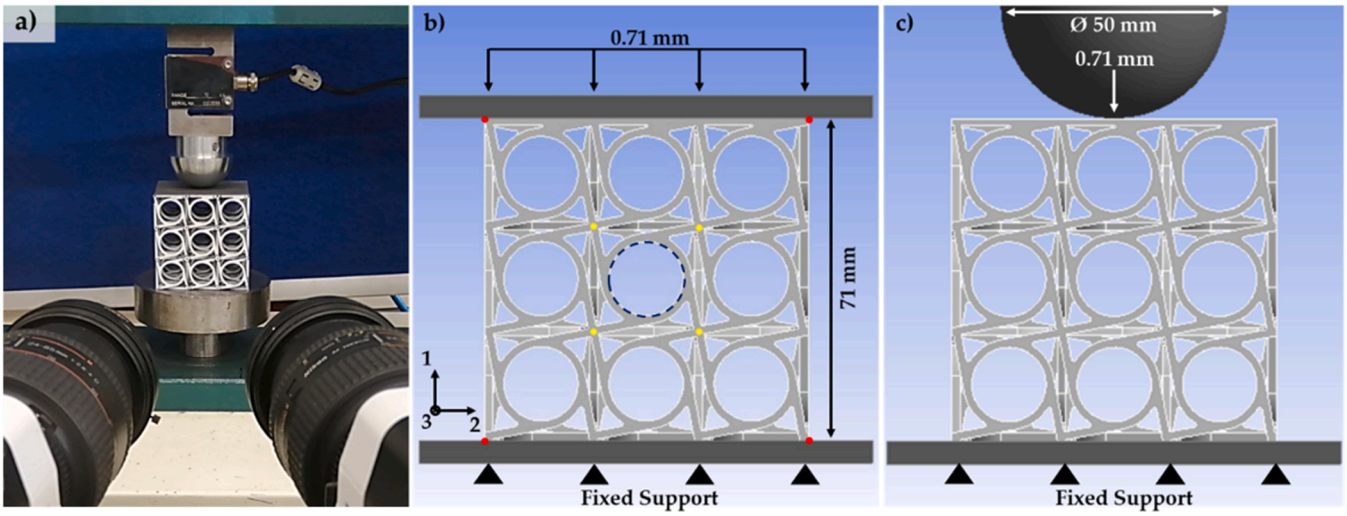

Fig. 2. a) Experimental indentation set up, and b) and c) simulation set up; b) flat plate and c) indentation. Axis labelling convention in (b) is used throughout. Red dots in (b) show lattice corner points tracked in the simulation and experiment, yellow dots show unit cell corner points tracked in the experiment, and the blue dashed line shows the edge at the centre of each face tracked in simulations.

similar [17]. So, for the effective point load caused by the indenter, the bending radius would be expected to be equal to l_c when $I_N = 1$. Irrespective of indenter size, the radius of curvature of the top sheet, which we name effective spherical indentation radius (R*), was:

$$R^* = l_c \times I_N \tag{18}$$

(i.e., $R^* = 2.6 \times 9.3 \approx 25$ mm). Varying the thickness of the top sheet between 1 and 2 mm, to vary I_N between 1 and 6, the relationship in Eq. 18 was maintained (within 3 % for $I_N > 2.6$ – see Supplementary information S5).

Quasi-static tests at a rate of 2.85 mm/minute to 1 % compression (~0.71 mm), and indentation tests with a 50 mm diameter hemisphere

to the same depth, were undertaken on a uniaxial test device (Hounsfield HK10s, 10 kN load cell, Fig. 2). The hemisphere was selected to match the expected curvature of the top surface (based on Eq. 18) to avoid stress concentrations (see supplementary Fig. S6d). One test was undertaken per lattice per condition, with a preload of 50 N for compression tests (~10 % of maximum compression force), reduced to 5 N for the indentation tests (~10 % of maximum indentation force). Tests were filmed by two synchronised cameras (Phantom Miro, R111 & Nikon, AF Nikkor 14,585 mm lens, 1200 × 800p, 24 Hz – Fig. 2a), and deformations of the front face of lattices were measured by stereo (3D) digital image correlation (DIC, GOM Correlate Professional, 2018 – Carl Zeiss GOM Metrology, GmbH, Braunschweig, Germany). GOM's CP20/MV 72 × 90 mm calibration board was used following supplier guidelines, and black dots on (white) lattice corners and the corners of the central unit cell were tracked by the software (Fig. 2b). Axial deformation was calculated from vertical movement of dots in the corners of lattices. A force constant for compression and indentation tests was obtained by fitting lines to force vs. displacement data – with DIC displacement used during compression tests and device displacement during indentation. Only the final linear region – 0.15 mm applied displacement – of each test was analysed, removing sections affected by uneven contact between the compression plate/indenter and lattice, due to printing imperfections. Micropolar Young's modulus, Poisson's ratio and twist results, used to validate the FE simulations, are shown in Supplementary information S3. The ~20 % differences between simulations and experimental data are attributed to warping and other imperfections on printed lattice surfaces, experimental error, and assumptions in the FE model.

2.4. Finite element methods

The tests were also simulated in a finite element model (ANSYS Workbench Mechanical (Static Structural), v2021 R2 (Livermore Software Technology Corporation, CA, USA)). An isotropic, linear elastic material model was used based on measured (ASTM D638-14 [50]) Nylon-12 properties for printed samples (E = 1.79 GPa, $\nu = 0.37$, density = 982 kg/m^3, Supplementary information S2, which were as expected [51,52]). A tetrahedral (solid element) mesh, with an element size of 0.9 mm, was applied to the lattices (Supplementary information S4 for mesh convergence study). The mesh was refined by defining contact and surface sizing around the indenter (0.5 mm over the contact region, and half the top sheet thickness over the top sheet). The compression plates and indenter were assigned steel (E = 200 GPa, $\nu = 0.3$), and an element size of 2.5 mm. A low co-efficient of friction (of 0.1) was defined between the lattice and compression plates/indenter, which was close to the assumed frictionless calculations (Eqs. 1 to 17). The results were cross-checked against those for the typical value for nylon on steel of 0.5 [53] (Supplementary information S3). The simulations with a co-efficent of friction of 0.1 and 0.5 were expected to match more closely to the calculations and experimental values, respectively. During the simulations of flat plate compressions, twist angle and deformation were recorded at the eight lattice corners, and the centre of lattice sides, respectively (Fig. 2b). Torsional tests were also simulated, by fixing plates to the lattices and applying a remote rotation (φ) of 1° – measuring the applied moment (T). Torsional modulus (G_t) was:

$$G_t = \frac{Tl}{\varphi J} \tag{12}$$

whereby l was lattice height, and J was the polar second moment of area. See Supplementary information S6 for torsional simulation details.

Equivalent lattices were modelled using beam elements, to show the effect of varying the size (and number) of unit cells without substantially increasing the computational requirements of the simulations. Maintaining the same overall dimensions and unit cell shape as in Fig. 1a & c, the number of unit cells were 1, 3, 5 or 7 per side (i.e., 1–343 unit cells, with ~10 to ~70 mm sides). As in prior work [30], the critical length did not change with unit cell size while maintaining lattice dimensions. Beams were extracted from modified lattices, topology was shared between all beam elements, and a midplane shell was used to replace the top sheet (in ANSYS Space Claim). Circular cross-sectional areas of 1.5 mm were set for the three unit-cell sided lattice to maintain the second moment area of the beams, edited to maintain lattice density (in ANSYS Mechanical). Pinball radii (boundary between open and closed contact) of 1 mm were applied to contacts, and effective top sheet thickness was set to 1.5 mm. Beam elements had a maximum mesh size equal to their diameter, to maintain an aspect ratio (length/diameter) of 1 (with <1.5 % change in maximum compression force as element size increased by double or decreased by 50 %). The top sheet surface elements had a maximum mesh size of 0.75 mm.

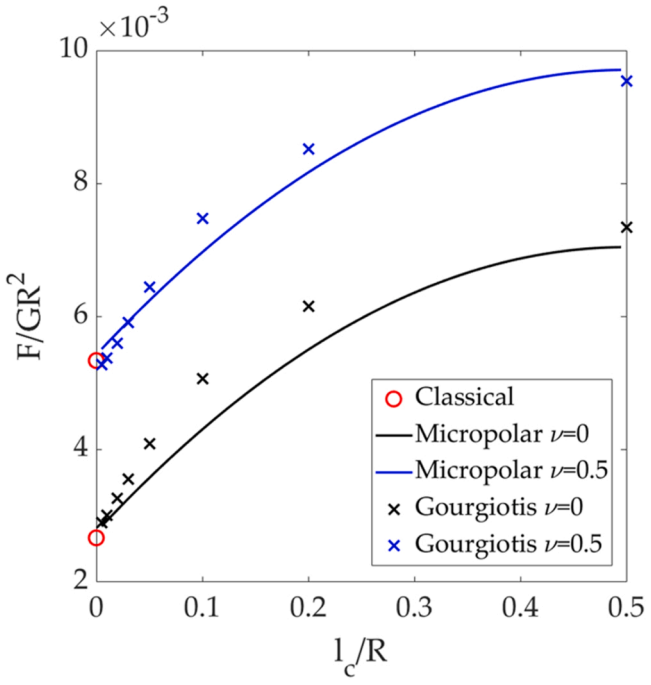

Fig. 3. Comparison between Eq. (14) and previous theoretical exploration of the Hertz contact in couple-stress elasticity [46].

3. Results

The micropolar 2D plane stress methods used here show reasonable fit (within 10 %) with data from a previous (3D) exploration of Hertzian contact in couple-stress elasticity (Fig. 3).

During compression, the lattices behaved as expected; the chiral ones twisted (Fig. 4a) and the antichiral ones did not (Fig. 4b). The upper half of the chiral lattice rotated clockwise, and the bottom half rotated anticlockwise (when viewed from above). The deformation amplification (scale factor of 10) used to clearly show shape change created the false appearance of cell rib buckling, which was not present without amplification, nor during the experiments (e.g., Supplementary Fig. S3). The total twist angle was up to 1.3° per 1 % strain (Table 1). The antichiral lattice bulged (Fig. 4a), while the $\theta = 34.3°$ chiral lattice contracted transversely (Fig. 4b); respective positive and negative Poisson's ratio (auxetic) behaviour. The micropolar Young's modulus (E_m) of the chiral (34.3°) lattice was ~50 % lower than that of the antichiral (0°) one (Table 1), and the magnitude of the chiral lattice's Poisson's ratio (ν_m) was also lower. As we varied rib thickness to maintain lattice mass, rather than maintain rib second moment of area, those with solid elements were stiffer than those with beam elements (Table 2).

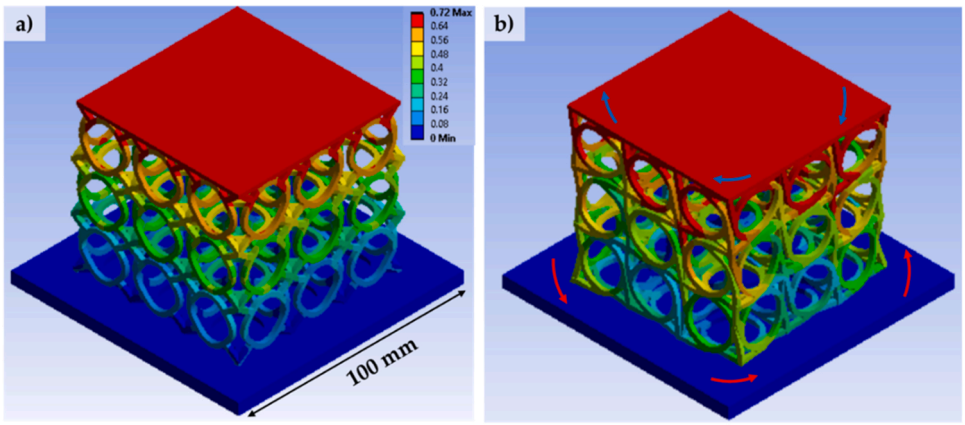

Fig. 4. Resultant deformation of a) antichiral, and b) chiral lattices at 1 % compression (deformation scale factor of 10, same legend (a) for both). Annotations added to (b) to show lattice twist direction. Top compression plate hidden.

Table 1
Lattice characteristics from simulations – G_m was calculated from E_m and ν_m.

Angle (θ°)	34.3	30	25	20	10	0
E_m (MPa)	9.57	10.51	11.49	12.41	14.32	14.98
G_m (MPa)	5.27	5.22	5.26	5.40	6.04	6.25
G_t (kPa)	1.49	1.01	0.76	0.63	0.52	0.51
ν_m	-0.09	0.07	0.09	0.11	0.19	0.20
Twist (° per 1 %)	1.30	1.02	0.61	0.29	0.14	0.01
l_w (mm)	17.90	14.10	8.30	4.00	1.90	0.00
α (MPa/m)	166.9	130.3	77.2	39.4	20.6	1.9
Mass (grams)	36.1	34.9	34.1	33.7	33.1	33.0

Table 2
Lattice characteristics from beam element simulations.

Unit cells/side	1	3	5	7
E_m (MPa)	4.91	5.92	4.33	3.85
G_m (MPa)	3.59	3.67	2.94	2.26
G_t (kPa)	4.73	3.21	2.18	1.02
ν_m	-0.09	0.07	0.09	0.11
Twist (° per 1 %)	0.67	0.88	0.80	0.63
A ($mm^2 \times 10^{-3}$)	71.0	23.2	13.9	9.9
l_w (mm)	9.3	12.2	11.0	8.8
α (MPa/m)	6.52	79.0	158.2	191.0

Normalising to flat plate compression force, noting that the magnitude of Poisson's ratio was lower for the twisting than for the non-twisting lattices (Table 1), twist increased relative indentation force by ~70 % (Fig. 5a). Relative experimental indentation force followed the same trend as the simulations but was ~10 % higher (Fig. 5a). Eq. (10) predicted indentation force to within 7 % of the simulations (Fig. 5a), tending to match more closely as twist increased. Classical Hertzian indentation force predictions (using the Cauchy plane stress modulus, Eq. 2) do not include twist, so did not follow the trend of indentation resistance increasing with the amount of twist (Fig. 5a), as expected. The Hertzian indention force of the non/low-twisting lattices ($\theta \leq 10°$) was within ~10 % of simulation and experimental values, and within 2 % of the micropolar calculations – within rounding errors. Similar fit (within ~10 %) between simulation (beam element model) and micropolar calculation was seen for various unit cell sizes (Fig. 5b). The increasing relative force with the number of unit cells was due to a higher effective radius (I_N was highest for the seven cell sided lattice).

4. Discussion

Experimental, simulation, micropolar and Willis values for relative indentation force agree (Fig. 5). Fig. 3 also shows that the micropolar plane stress methods agree with 3D methods [46], with the cases herein broadly meeting the assumption that twist caused an axisymmetric response so lattices could be homogenised in 2D. The limitations to axisymmetry, found here to have a small effect on analysis results, were

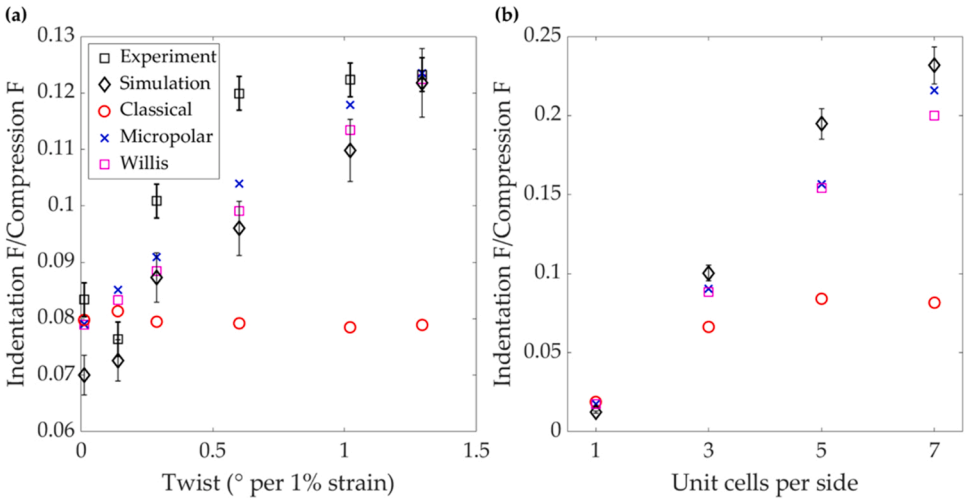

Fig. 5. Normalised indentation force vs. a) twist angle per 1 % strain, and b) unit cells per side, from solid (a) and beam (b) element finite element simulations, micropolar calculations (Eq. 14), Willis calculations (Eq. 17) and classical Hertzian contact (Eq. 3), which does not include twist but is included for each sample for comparison. Experimental error bars show minimum load cell precision ($\pm$ 0.33 N, or $\pm 3 \times 10^{-3}$), simulation error bars show mesh convergence error (1.5 % of force, or $\pm 5 \times 10^{-3}$). Same legend for (a) and (b).

i) twist caused variable sign (but not magnitude) of deformation on opposing sides, and ii) lattice unit cell isotropy was triaxial (cubic), not axisymmetric. The Hertzian contact mechanics assumptions of isotropy [17], elasticity (Supplementary Fig. S9, showing no visible damage to the lattice), and relationships between indenter and sample size, were broadly met (ASTM D3574 – 11 - [49]).

The experimental data's discrepancy in relative indentation resistance was attributed to the low number of tests (one per condition / lattice design) and warping of the top and bottom of lattices during printing, causing lower than expected micropolar Young's moduli (Supplementary information S3). Warping was most evident in the outlying lattice with ~0.6° of twist per 1 % strain (Fig. 5a), and its effect was noticeable, because the deformations were relatively low. While we used Nylon-12, to allow precise printing by selective laser sintering, an alternative approach that may be useful in further work would be to print lattices with a hyperplastic material, for testing to a larger depth. Options to precisely fabricating flexible 3D lattices are becoming increasingly accessible [54–56]. Inclusion of a flexible material around cell junctions, and rigid material within the cell, could also increase control over the amount of twist [57].

The lattices were assumed to deform as continuum solids – which may have also caused discrepancies. Lattices with few unit cells were required here because; i) twist reduces with more unit cells [30]; ii) we approached the limits of the manufacturing and testing equipment (Formlabs Fuse 1). Fit between Eqs. (14) and (17), and the simulation data, were insensitive to the number of unit cells in the lattice (Fig. 5b). Our approach differed from the previous one using nanoscopic indenters to achieve high ratios of internal length scales to contact radius [43–47]. While we had control over lattice stiffness, twist and Poisson's ratio, we had to create a solid, connected upper surface for the indenter to load. The indenter then acted as a point load, creating a curved, approximately spherical, surface (see supplementary Fig. S6d). While the effect of changing the top sheet could be explained by Eq. (18) (see supplementary Fig. S7b), varying the indenter size had little effect, because the contact radius was smaller than the effective radius (Eq. 18). Similarly, we would not expect the effective radius to change if another shape (e.g., punch or cone) were used to apply the indentation, although these may have caused high pressure zones and local plasticity.

To allow an idealised study into the indentation of twisting materials, without the need for a top-sheet and correction according to Eq. (18), further work could develop quasi-continuum twisting structures (e.g., [58]). Such quasi-continuum structures, either with small unit cells or large external dimensions, would be more complex to make and test, respectively. While these may not be commercially viable, development of the underlying theory remains important, with implications for the analysis of biological tissue [30,31], composites [32–34], other lattices or mechanical metamaterials [59–61], or foams where twisting occurs within cells (rather than externally) [62]. Conversely, testing such materials may provide another option to develop the theory, although with less twist the effect sizes would be smaller, placing greater requirements on experimental accuracy.

The simulation, experiment and calculation findings all follow similar trends, with the implication that relative indention resistance increased with twist. The classical indentation Eqs. (1 to 3), and those we applied to indentation for the first time here (Eqs. 8 to 17), use the 2D approximation for plane stress modulus. Eqs. (8) to (17) provide an intuitive link between variables (such as indentation depth and radius), material properties (such as Young's modulus, Poisson's ratio and twist) and indentation force. They remain relatively untested during indentation of twisting materials, and the limits of application of the method of dimensional reduction could still be explored. Further work could apply or develop Eqs. (8) to (18), or other 3D analysis methods [43–47], for off-centre contact with the unit cells, non-symmetric indenters, or anisotropic materials, where deformations in the third axis may be imbalanced. Such work could facilitate better understanding of the effect of twist during indentation, and inform the design of simpler to make, 2D extruded (orthotropic) twisting lattices.

We used small strains and indentation depths, while much of the previous work on mechanical metamaterials focusses on impact – with high indentation rates, and large depths/strains [10,63–65]. The Willis methods presented here are well suited to analysis of elasto-dynamic events [36,37], but have not been developed to account for strain regions with non-linear behaviour. These methods required a lower number of additional variables (α and l_w), making characterisation and analysis simpler, but these variables required some estimation [38]. Conversely, micromorphic methods, more similar to the micropolar ones used here, have been extended to large strains [66], and the additional variables can be measured [35]. With more tensors, analysis can become complex, or a source of compiled errors; selecting the most appropriate method could affect analysis cost and accuracy.

Showing that twist increases hardness provides options for fundamental and applied research. As with auxetic materials [3,10,67], twisting materials could provide benefits during impact. While transverse contraction of conventional auxetics during compression can cause earlier densification [68], twist would not. During impact, early densification of padding is associated with higher risk of damage or injury [10,69,70], and twist is an alternative counterintuitive hardening mechanism that reduces such risks. Twist/compression (or extension) is a coupled term, meaning that twisting a material with twist/-compression coupling causes either extension or compression. So, twist could also provide a tuneable response to torsional fretting – where twist between contacting bodies causes surface damage [71], with applications from human joints to car suspension [72]. Targeting twist as a counterintuitive hardening mechanism could become a research focus spanning mechanical metamaterials, solid/continuum mechanics, experimental mechanics and applied mathematics, with potential cross-sector applications. Demonstrating and validating analysis methods for twisting materials, so they can be efficiently modelled as continuum rather than microstructurally faithful materials, is an important step in their realisation.

5. Conclusion

Twist caused a ~70 % increase in normalised indentation force over a similar non-twisting lattice. While Poisson's ratio varied between the twisting and non-twisting lattices, the magnitude of Poisson's ratio was highest for the non-twisting lattice, so the changing Poisson's ratios are unlikely to have affected the findings (Eq. 2). Calculating micropolar (Eq. 8) and Willis (Eq. 15) plane stress moduli allowed prediction of indentation force (Eq. 14 & 17) to within 10 % of simulation and experimental values. Micropolar methods were more complex but more rigorous, while Willis methods were more efficient (requiring fewer variables). Twist can be considered a potentially beneficial hardening mechanism, opening a new field of study spanning contact mechanics, micropolar/higher order elasticity and mechanical metamaterials.

CRediT authorship contribution statement

Dr Duncan conceptualised and designed the study, undertook the experiments, simulations and calculations, and wrote the manuscript. Dr **Allen** and Prof **Alderson** provided feedback during study design and writing. Dr Wang provided feedback on the indentation calculations. Mr **Chester** printed the lattices.

Declaration of Competing Interest

The authors declare that they have no known competing financial interests or personal relationships that could have appeared to influence the work reported in this paper.

Data availability

Numerical results, MATLAB analysis scripts and STL files of all lattices are available via. Mendeley data (Duncan, Olly; Chester, Mark; Wang, Weizhuo; Alderson, Andrew; Allen, Tom (2023), "Data for "Effect of twist on indentation resistance"", Mendeley Data, V1, doi: 10.17632/pvpwzmknfj.1). All other data will be made available upon reasonable request. Simulation and digital image correlation files will be stored on a secure server until 2026.

Acknowledgements

We would like to thank the technical services staff at Manchester Metropolitan University for their help with the experiments and lattice preparation – particularly Mr Green, Mr Dickenson and Mr Thomas. We would also like to thank our colleagues Prof Liskiewicz and Dr Teklemariam, and the reviewers and editors, for providing feedback on the manuscript.

Appendix A. Supporting information

Supplementary data associated with this article can be found in the online version at doi:10.1016/j.mtcomm.2023.105616.

References

[1] N. Chan, K.E. Evans, Indentation resilience of conventional and auxetic foams, J. Cell. Plast. 34 (1998) 231–260.
[2] K.L. Alderson, A. Fitzgerald, K.E. Evans, The strain dependent indentation resilience of auxetic microporous polyethylene, J. Mater. Sci. 35 (16) (2000) 4039–4047.
[3] K.E. Evans, A. Alderson, Auxetic materials: functional materials and structures from lateral thinking!, Adv. Mater. 12 (9) (2000) 617–628.
[4] U. Mawkhlieng, A. Majumdar, Soft body armour, Text. Prog. 51 (2) (2019) 139–224.
[5] K.B. Bhagavathula, A. Azar, S. Ouellet, S. Satapathy, C.R. Dennison, J.D. Hogan, High rate compressive behaviour of a dilatant, Polym. Foam. J. Dyn. Behav. Mater. 4 (4) (2018) 573–585.
[6] Dolez P.I., Mlynarek J. , Smart Materials for Personal Protective Equipment: Tendencies and Recent Developments, Elsevier Ltd, (2016), 497–517.
[7] A. Majumdar, B.S. Butola, A. Srivastava, Development of soft composite materials with improved impact resistance using Kevlar fabric and nano-silica based shear thickening fluid, J. Mater. 54 (2014) 295–300.
[8] Y. Wang, L. Li, D. Hofmann, J.E. Andrade, C. Daraio, Structured fabrics with tunable mechanical properties, Nature 596 (7871) (2021) 238–243.
[9] V.A. Lvov, F.S. Senatov, A.A. Veveris, V.A. Skrybykina, A.D. Lantada, Auxetic metamaterials for biomedical devices: current situation, main challenges, and research trends, Materials (2022) 15.
[10] O. Duncan, T. Shepherd, C. Moroney, L. Foster, P.D. Venkatraman, K. Winwood, et al., Review of auxetic materials for sports applications: expanding options in comfort and protection, Appl. Sci. 8 (6) (2018) 941.
[11] S. Mohsenizadeh, R. Alipour, M. Shokri Rad, A. Farokhi Nejad, Z. Ahmad, Crashworthiness assessment of auxetic foam-filled tube under quasi-static axial loading, Mater. Des. 88 (2015) 258–268.
[12] H.M.A. Kolken, A.A. Zadpoor, Auxetic mechanical metamaterials, RSC Adv. 7 (2017) 5111–5129.
[13] K.L. Alderson, A.P. Pickles, P.J. Neale, K.E. Evans, Auxetic polyethylene: the effect of a negative Poisson's ratio on hardness, Acta Metall. Mater. 42 (7) (1994) 2261–2266.
[14] H.R. Hertz, D. Jones, G. Schott, Miscellaneous Papers, Macmillan Co. Ltd., 1896, pp. 156–171.
[15] V.L. Popov, M. Heß, E. Willert, Handbook of Contact Mechanics: Exact Solutions of Axisymmetric Contact Problems (2019), 7-10,12.
[16] Popov V.L. , Contact Mechanics and Friction, Springer Berlin Heidelberg, Berlin (2010),19, 60, 62, 68, 69, 250.
[17] S.P. Timoshenko, J.N. Goodier, Theory of Elasticity, third ed., McGraw-Hill, New York, USA, 1970.
[18] A. Schiavi, C. Origlia, A. Germak, A. Prato, Indentation modulus , indentation work and creep of metals and alloys at the macro-scale level : experimental insights into the use of a primary vickers hardness standard machine, Materials (2021).
[19] J. Prou, K. Kishimoto, A. Constantinescu, Identification of Young's modulus from indentation testing and inverse analysis, J. Solid Mech. Mater. Eng. 4 (6) (2010) 781–789.
[20] D.C. Lin, D.I. Shreiber, E.K. Dimitriadis, F. Horkay, Spherical indentation of soft matter beyond the Hertzian regime: numerical and experimental validation of hyperelastic models, Biomech. Model. Mechanobiol. 8 (5) (2009) 345–358.
[21] K. Johnson, Contact Mechanics, Cambridge University Press, Cambridge, UK, 1985.
[22] V.L. Popov, E. Willert, M. Heß, Method of Dimensionality Reduction in Contact Mechanics and Friction: a User's Handbook. iii. Viscoelastic Contacts, 16. (2018),19.
[23] I. Argatov, A discussion of the method of dimensionality reduction, Proc. IMechE Part C. J. Mech. Eng. Sci. 230 (9) (2016) 1424–1431.
[24] K.M. Knowles, The plane strain Young's modulus in cubic materials, J. Elast. 128 (2017) 147–173.
[25] Johnson K.L. , Line loading of an elastic half-space, in: Contact Mechanics, Cambridge University Press, Cambridge, UK (1985), 11–44.
[26] R.S. Lakes, Foam structures with a negative Poisson's ratio, Science 80- (4792) (1987) 1038–1040, 235.
[27] A.C. Eringen, Linear theory of micropolar viscoelasticity, Int. J. Eng. Sci. 5 (2) (1967) 191–204.
[28] S.C. Cowin, Stress functions for cosserat elasticity, Int. J. Solids Struct. 6 (1970) 389–398.
[29] S. Nakamurat, R.S. Lakes, Finite element analysis of saint-venant end effects in micropolar elastic solids, Eng. Comput. 12 (6) (1995) 571–587.
[30] T. Frenzel, M. Kadic, M. Wegener, Three-dimensional mechanical metamaterials with a twist, Science 80- (6366) (2017) 1072–1074, 358.
[31] I. Fernandez-Corbaton, C. Rockstuhl, P. Ziemke, P. Gumbsch, A. Albiez, R. Schwaiger, et al., New twists of 3D chiral metamaterials, Adv. Mater. 31 (26) (2019) 1–7.
[32] York C.B. , Extension-twist coupled laminates for aero-elastic compliant blade design, in: Proceedings of the Fifty Third AIAA/ASME/ASCE/AHS/ASC Structures, Structural Dynamics and Materials Conference, 20th AI 23–26 April, 2012, Honolulu, Hawai (2012), 1–22.
[33] R.C. Lake, M.W. Nixon, M.L. Wilbur, J.D. Singleton, P.H. Mirick, A demonstration of passive blade twist control using extension-twist coupling, Aerosp. Res. Cent. 92 (2468) (1992) 774–781.
[34] M.W. Nixon, Extension-twist coupling of composite circular tubes with application to tilt rotor blade design, Aerosp. Res. Cent. 87 (0772) (1987) 295–303.
[35] R.D. Gauthier, W.E. Jahsman, A quest for micropolar elastic constants, J. Appl. Mech. Trans. ASME 42 (2) (1975) 369–374.
[36] J.R. Willis, Elasticity Theory of Composites, Pergamon Press Ltd,, 1982, pp. 653–686, https://doi.org/10.1016/B978-0-08-025443-2.50025-2.
[37] G.W. Milton, M. Briane, J.R. Willis, On cloaking for elasticity and physical equations with a transformation invariant form, New J. Phys. (2006) 8.
[38] M. Kadic, A. Diatta, T. Frenzel, S. Guenneau, M. Wegener, Static chiral Willis continuum mechanics for three-dimensional chiral mechanical metamaterials, Phys. Rev. B 99 (21) (2019) 1–6.
[39] M.A. Wheel, A control volume-based finite element method for plane micropolar elasticity, Int. J. Numer. Methods Eng. 75 (2008) 992–1006.
[40] Cosserat E., Cosserat F. , Théorie des Corps Deformables, Hermann et Fils, Paris, France (1909).
[41] Eringen A.C. , Microcontinuum Field Theories, first ed., Springer Science+Business Media, New York (1999).
[42] A.C. Eringen, Theory of micropolar elasticity. Microcontinuum Field Theories, Springer, New York, 1999, pp. 101–248.
[43] G. Pierson, M. Taghite, P. Bravetti, R.K. Njiwa, Spherical indentation of a micropolar solid: a numerical investigation using the local point interpolation–boundary element method, Appl. Mech. 2 (3) (2021) 581–590.
[44] T. Zisis, P.A. Gourgiotis, Cylindrical indentation in micropolar elasticity, Appl. Math. Model. 104 (2022) 373–385.
[45] S. Hassan Salehi, M. Salehi, Finite element study for conical indentation of elastoplastic micropolar material, Int. J. Solids Struct. 51 (23–24) (2014) 3987–3995.
[46] P.A. Gourgiotis, T. Zisis, A.E. Giannakopoulos, H.G. Georgiadis, The Hertz contact problem in couple-stress elasticity, Int. J. Solids Struct. 168 (2019) 228–237.
[47] T. Zisis, P.A. Gourgiotis, K.P. Baxevanakis, H.G. Georgiadis, Some basic contact problems in couple stress elasticity, Int. J. Solids Struct. 51 (11–12) (2014) 2084–2095.
[48] McGregor M., Wheel M.A. , On the coupling number and characteristic length of micropolar media of differing topology, Proc. R. Soc. A Math. Phys. Eng. Sci., (2014).470(2169).
[49] Annual Book of ASTM Standards, Standard test methods for flexible cellular materials — slab, bonded, and molded urethane foams, Annual Book of ASTM Standards 2008.
[50] American Society for Testing and Materials, ASTM D638 - 14: Standard Test Method for Tensile Properties of Plastics, ASTM Int. (2016).82(C), 1–15.
[51] MatWeb, Overview of materials for Nylon 12 (2022). https://www.matweb.com/search/datasheet.aspx?matguid=0e37a459c4eb452faa9d92659f9a0ccc&ckck=1. (Accessed17 March 2022).
[52] Formlabs , Formlabs Nylon 12 Technical Datasheet (2020). https://formlabs-media.formlabs.com/datasheets/2001447-TDS-ENUS-0.pdf. (Accessed17 March 2022).
[53] M. Watanabe, M. Karasawa, K. Matsubara, The frictional properties of nylon, Wear 12 (3) (1968) 185–191.
[54] X. Zheng, X. Guo, I. Watanabe, A mathematically defined 3D auxetic metamaterial with tunable mechanical and conduction properties, Mater. Des. 198 (2021), 109313.
[55] S. Yuan, F. Shen, J. Bai, C.K. Chua, J. Wei, K. Zhou, 3D soft auxetic lattice structures fabricated by selective laser sintering: TPU powder evaluation and process optimization, Mater. Des. 120 (2017) 317–327.
[56] A. Ronca, G. Rollo, P. Cerruti, G. Fei, X. Gan, G.G. Buonocore, et al., Selective laser sintering fabricated thermoplastic polyurethane/graphene cellular structures with tailorable properties and high strain sensitivity, Appl. Sci. 9 (5) (2019) 1–15.

[57] K. Wang, Y.H. Chang, Y. Chen, C. Zhang, B. Wang, Designable dual-material auxetic metamaterials using three-dimensional printing, Mater. Des. 67 (2015) 159–164.
[58] T. Frenzel, V. Hahn, P. Ziemke, J.L.G. Schneider, Y. Chen, P. Kiefer, et al., Large characteristic lengths in 3D chiral elastic metamaterials, Commun. Mater. 2 (1) (2021) 1–9.
[59] T. Shepherd, T. Allen, K. Winwood, P.D. Venkatraman, A. Alderson, Validation of a finite element modelling process for auxetic structures under impact, Phys. Status Solidi B Basic Solid State Phys. (2020) 1900197.
[60] B. Hanna, R. Adams, S. Townsend, M. Robinson, S. Soe, M. Stewart, et al., Auxetic metamaterial optimisation for head impact mitigation in American football, Int. J. Impact Eng. 157 (2021), 103991.
[61] R. Adams, S. Townsend, S. Soe, P. Theobald, Finite element-based optimisation of an elastomeric honeycomb for impact mitigation in helmet liners, Int. J. Mech. Sci. 214 (2022), 106920.
[62] R. Lakes, W.J. Drugan, Bending of a cosserat elastic bar of square cross section: theory and experiment, J. Appl. Mech. Trans. ASME 82 (9) (2015) 1–16.
[63] J.U. Surjadi, L. Gao, H. Du, X. Li, X. Xiong, N.X. Fang, et al., Mechanical metamaterials and their engineering applications, Adv. Eng. Mater. 21 (3) (2019) 1–37.
[64] P.U. Kelkar, H.S. Kim, K.H. Cho, J.Y. Kwak, C.Y. Kang, H.C. Song, Cellular auxetic structures for mechanical metamaterials: a review, Sensors 20 (11) (2020) 1–26.
[65] K.K. Saxena, R. Das, E.P. Calius, Three decades of auxetics research – materials with negative Poisson's ratio: a review, Adv. Eng. Mater. 18 (11) (2016) 1847–1870.
[66] S. Forest, Micromorphic approach for gradient elasticity, viscoplasticity, and damage, J. Eng. Mech. 135 (3) (2009) 117–131.
[67] N. Novak, M. Vesenjak, Z. Ren, Auxetic cellular materials - a review, Stroj Vestn. /J. Mech. Eng. 62 (9) (2016) 485–493.
[68] M. Wallbanks, M.F. Khan, M. Bodaghi, A. Triantaphyllou, A. Serjouei, On the design workflow of auxetic metamaterials for structural applications, Smart Mater. Struct. 31 (2) (2022).
[69] Ashby M.F., Evans A.G., Fleck N.A., Gibson L.J., Hutchinson J.W., Wadley H.N.G. , Metal Foams: a Design Guide, Butterworth-Heinemann, Boston, US (2000),151–156.
[70] R. Wu, P.C.E. Roberts, S. Lyu, F. Zheng, C. Soutis, C. Diver, et al., Lightweight self-forming super-elastic mechanical metamaterials with adaptive stiffness, Adv. Funct. Mater. (2020) 2008252.
[71] M.H. Zhu, Z.R. Zhou, On the mechanisms of various fretting wear modes, Tribol. Int. 44 (11) (2011) 1378–1388.
[72] G. Costagliola, F. Bosia, N.M. Pugno, Tuning of frictional properties in torsional contact by means of disk grading, Friction 10 (5) (2022) 787–802.